

# Atmospheric characterization of the Sub-Neptune exoplanet K2-18b: A Bayesian analysis of its possible structure and composition

Juan Zapata-Marin<sup>1\*</sup>, Pablo Cuartas-Restrepo<sup>1</sup>

<sup>1</sup>*Grupo FAcOm - Instituto de Física - FCEN, Universidad de Antioquia, Medellín, Colombia.*

Accepted 2025 March 27. Received 2025 March 17; in original form 2024 December 6

## ABSTRACT

K2-18b is a temperate habitable-zone Sub-Neptune that has attracted significant interest due to its potential to host a H/He-rich envelope and to contain H<sub>2</sub>O traces in its atmosphere. Transmission spectroscopy with JWST has revealed the presence of the carbon-bearing molecules CH<sub>4</sub> and CO<sub>2</sub> along with the non-detection of NH<sub>3</sub>, aligning with the "Hycean" world scenario, which consists of a shallow H<sub>2</sub>-dominated atmosphere overlaying a potentially liquid water surface ocean, creating optimal conditions that favour habitability. Recent studies have proposed alternative scenarios compatible with observations, including a mini-Neptune scenario with a deep atmosphere and no well-defined surface, or a lava world scenario consisting of a molten magma ocean on its surface. Here, we report a Bayesian retrieval analysis of K2-18b's transmission spectrum, exploring several models for its chemical composition, temperature profile, and cloud properties. We evaluate a set of not self-consistent atmospheric retrievals aiming to constrain the atmospheric properties, examining the detection significance of key molecular species and investigating how grey and non-grey cloud treatments impact the inferred structure and composition. For both cloud treatments, we find detection significances for CH<sub>4</sub> and CO<sub>2</sub> of 5  $\sigma$  and 3 $\sigma$  respectively, while finding no significant evidence for H<sub>2</sub>O and NH<sub>3</sub>, in agreement with previous studies. Additionally, we find that a cloud-free atmosphere for K2-18b is strongly ruled out by observations. Our results suggest that a model consisting of non-grey cloud treatment and following a semi-ideal temperature-pressure profile provides the best fit to the observed spectrum.

**Key words:** Sub-Neptune exoplanets, transmission spectroscopy, planetary atmospheres, atmospheric retrievals, K2-18b

## 1 INTRODUCTION

Sub-Neptunes are a diverse class of exoplanets with intermediate sizes and masses between Earth and Neptune, typically spanning radii between 1.8 and 3.6  $R_{\oplus}$  and masses between 2 and 10  $M_{\oplus}$  (Rogers 2014). These planets are large enough to retain substantial H/He-rich envelopes, similar to the ice giants in our solar system. Observations indicate that Sub-Neptunes are the most common type of exoplanets (Batalha 2014), even though no such planets exist in our own solar system. In recent years, JWST has provided unprecedented high-quality observations, enabling significant advancements in our understanding of Sub-Neptunes formation, composition, and evolutionary processes. These breakthroughs are crucial for studying the nature of these abundant but yet enigmatic planets.

A novel subset of exoplanets, known as Hycean planets, has been proposed within the population of Sub-Neptunes. These worlds are thought to be composed of a shallow H<sub>2</sub>-rich atmosphere and a water-rich interior, which could potentially exist as a surface liquid ocean (Madhusudhan et al. 2021). Hycean planets would be promising hosts for life beyond Earth as they may contain the essential conditions for habitability: energy, liquid water, and organic molecules. Due to their chemical composition, primarily dominated by volatiles such as H<sub>2</sub>, He or N<sub>2</sub>, these planets are expected to have low mean molecu-

lar weights, resulting in extended atmospheres that are particularly favourable for spectroscopic characterization. Beyond mass and radius, the atmosphere is the only observable feature of an exoplanet that provides insight into its thermal structure, chemical composition, and formation and evolution processes. The atmospheric properties of an exoplanet can be studied by analysing the spectrum of the light that it emits, reflects, or absorbs from its host star. Emission spectroscopy is relevant for highly irradiated exoplanets or those with significant internal heat sources, while transmission spectroscopy is applicable for transiting exoplanets, in which stellar flux filters through the atmosphere, revealing its composition.

The JWST telescope has provided exceptional access to the transmission spectra for dozens of exoplanets, spanning a wide range of sizes and properties, from ultra-hot Jupiters to Earth-sized planets. These spectra are obtained by comparing the host star's spectrum during and outside of the planetary transit. The multiple opacity sources present in the atmosphere cause the planet to appear larger at certain wavelengths, allowing one to infer its properties, structure, and composition in the day-night terminator region of the atmosphere.

Madhusudhan et al. (2023) reported the transmission spectrum of the Sub-Neptune K2-18b obtained with the NIRISS and NIRSPEC instruments of the JWST telescope in the range of 0.9–2.8  $\mu\text{m}$  and 2.8–5.2  $\mu\text{m}$  respectively. Through a data-driven Bayesian approach known as atmospheric retrieval (Madhusudhan & Seager 2009), they detected the presence of CH<sub>4</sub> and CO<sub>2</sub> in the K2-18b's atmosphere

\* E-mail: juan.zapata98@udea.edu.co

with a detection significance of  $5\sigma$  and  $2\sigma$  respectively, as well as the absence of spectral features of  $\text{NH}_3$  and  $\text{H}_2\text{O}$  in the atmospheric spectrum. Based on the detection of these molecules in the terminator region and the bulk density of the planet, they found that K2-18b spectrum exhibits acceptable evidence in favour of a Hycean scenario of a shallow  $\text{H}_2$ -rich atmosphere with significant traces of  $\text{CH}_4$  and  $\text{CO}_2$ , and with the presence of clouds/hazes in the atmosphere. Wogan et al. (2024) argue that a mini-Neptune scenario, with no habitable surface and a deep  $\text{H}_2$ -rich atmosphere presents similar evidence compared to the Hycean scenario and it's favoured in terms of model simplicity, as the latter would require the existence of a methanogenic biosphere to explain the high levels of  $\text{CH}_4$  detected.

Despite some planetary properties such as internal composition, thermal structure, or the undetection of spectral features of  $\text{H}_2\text{O}$  and  $\text{NH}_3$  in the spectrum remaining as unresolved problems, models that include clouds and/or hazes show favourable evidence compared to the cloud/haze free atmosphere models. Clouds and hazes play an important role in the atmospheres of temperate exoplanets, as they can contribute to atmospheric cooling and reduce the temperature gradient, allowing for more optimal conditions for the presence of a surface ocean compared to cloud/haze free atmospheres. However, current data for temperate exoplanets lack sufficient resolution and wavelength coverage necessary to model clouds in significant detail, limiting cloud models to grey cloud decks and preventing the possibility of fitting more complex models that account for the opacity dependence on wavelength.

In this work, we perform atmospheric retrievals on the JWST transmission spectrum of K2-18b to assess a wide variety of atmospheric models including different pressure-temperature profiles, chemical compositions, and cloud treatments. Additionally, an exploration of cloud models for K2-18b was conducted, which included grey and non-grey clouds with diverse parametrizations. The evaluation and comparison of models was carried out using the Bayesian evidence provided by the atmospheric retrieval framework. In Section 2, we provide a brief introduction to the atmospheric retrieval method. Section 3 describes the temperature-pressure profiles evaluated in the retrievals, while Section 4 details the evaluated cloud treatments. The chemistry treatments used to approach the chemical composition of the atmosphere are described in Section 5. In Section 6, we introduce the retrieval workflow and the strategy for Bayesian model comparison. The results of the retrievals, along with an analysis of the outcomes for each cloud treatment, are presented in Section 7. Finally, we summarize our findings in Section 8 and highlight the key conclusions of this study.

## 2 ATMOSPHERIC RETRIEVALS

Atmospheric modelling is carried out by defining a temperature-pressure profile, a chemical species population along with their abundances, and a physical model for the cloud/hazes properties, in what is known as a forward model. Atmospheric retrievals allow for the comparison of the observed spectrum with a large number of forward-generated spectra in order to find the model that best fits the data, thus solving the inverse problem of going from an observed spectrum to an atmospheric model consistent with the observations. Atmospheric retrievals use a random sampling algorithm to explore the full parameter space and find the set of parameters that best fits the measured spectrum (Madhusudhan & Seager 2009; Feroz et al. 2009). This framework also allows for the evaluation of various models composed of different parametrizations and approximations to the thermal structure, chemical composition, cloud coverage, and other

physical processes such as vertical mixing of atmosphere components or general circulation models (GCMs).

### 2.1 Nested Sampling algorithm

Retrievals are conducted using the petitRADTRANS package (Mollière et al. 2019), which employs the Nested Sampling algorithm implemented through the Pymultinest module (Feroz et al. 2009). This random sampling algorithm allows for efficient sampling of the full parameter space, similar to MCMC sampling methods, but with the advantage of providing a direct estimate of the marginal likelihood, which is very useful for model comparison and selection, while the sampling of posterior distributions turns out to be a natural by-product of the nested sampling algorithm.

From the Bayes' theorem, for data  $D$  and a set of parameters  $\theta$  of model  $M$ :

$$P(\theta | D, M) = \frac{P(D | \theta, M)P(\theta | M)}{P(D | M)} \quad (1)$$

where  $P(\theta | D, M) \equiv P(\theta)$  is the posterior distribution of parameters,  $P(D | \theta, M) \equiv \mathcal{L}(\theta)$  is the likelihood of the data,  $P(\theta | M)$  the prior distribution and  $P(D | M) \equiv Z$  the marginal likelihood or Bayesian evidence. This last term is the factor that normalizes the posterior over the parameters space:

$$Z = \int P(D | \theta, M)P(\theta | M) d\theta \quad (2)$$

The nested sampling algorithm (Feroz et al. 2009) proposes that by defining a *prior volume*  $X$  with  $dX = P(\theta | M) d\theta$ , then Equation 2 can be written as:

$$Z = \int_0^1 \mathcal{L}(X) dX \quad (3)$$

The algorithm proceeds by selecting a set of points from the prior, identifying the lowest likelihood sample, replacing it with a new sample of a higher likelihood, and updating  $X$  accordingly. This process results in an ordered sequence of likelihood values and corresponding decreasing prior volumes, which can be used to approximate  $Z$  with the weighted summation:

$$Z \approx \sum_i \mathcal{L}(X_i) \Delta X_i \quad (4)$$

where  $\Delta X_i$  represents the difference in prior volume between successive iterations. After the summation is terminated and the Bayesian evidence  $Z$  is determined, a posterior importance weight is assigned to each remaining and discarded point:

$$p_i \sim \frac{\mathcal{L}(X_i) \Delta X_i}{Z} \quad (5)$$

from which posterior distribution for each parameter can be reconstructed.

The algorithm starts by performing a prior-based random sampling of the parameters space, generating  $n$  sampled points known as *live points*. The likelihood function is evaluated at each live point, the one with the lowest likelihood  $\mathcal{L}_{\min}$  is discarded and then replaced with a new point with likelihood  $\mathcal{L}_j$  randomly sampled from the prior, requiring that  $\mathcal{L}_j > \mathcal{L}_{\min}$ , i.e., the new point must be contained within the iso-likelihood surface delimited by the old point

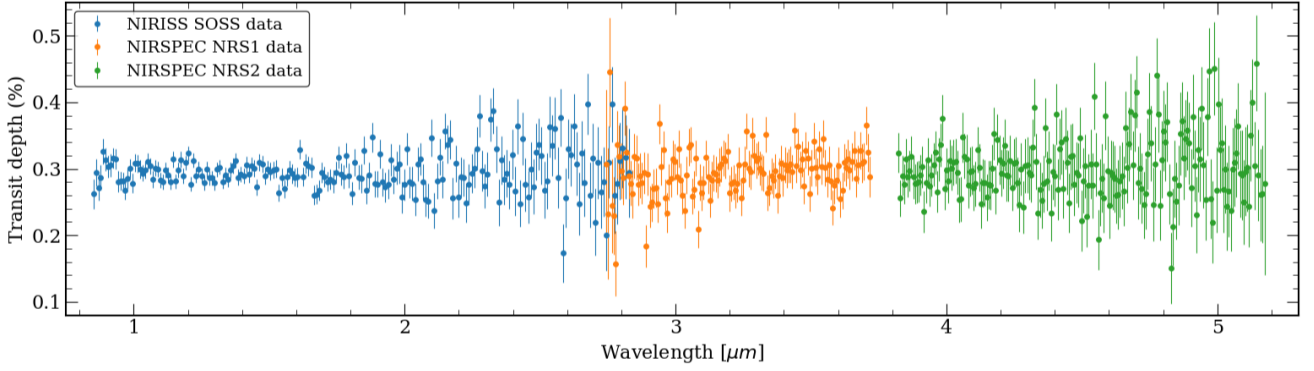


**Figure 1.** JWST transmission spectrum data of K2-18b from the NIRISS and NIRSPEC instruments. The data in the plot is a sample of the high-resolution spectrum reported in [Madhusudhan et al. \(2023\)](#). The lack of data near  $3.7 \mu\text{m}$  corresponds to the gap between NRS1 and NRS2 detectors of the NIRSPEC instrument.

likelihood  $\mathcal{L}_{\min}$ . As the algorithm iterates this procedure, the likelihood threshold increases and the volume shrinks. The iteration stops when the remaining live points are close enough to the best-fit parameter peak and the likelihood is flat, thus further integration has a negligible contribution.

### 3 PRESSURE-TEMPERATURE PROFILES

#### 3.1 Isothermal model

This is the simplest model that can be assumed for the temperature profile of an atmosphere. The temperature does not depend on pressure, and it is constant throughout the entire atmosphere:

$$T(P) = T_0 \quad (6)$$

#### 3.2 Guillot (2010)

A general temperature profile model for irradiated exoplanets, proposed by [Guillot \(2010\)](#). This semi-ideal model assumes that the incoming radiation field due to the stellar irradiation and the outgoing radiation field due to the thermal emission of the planet are strongly decoupled, so they can be treated separately and the source function can be determined for each of them. Despite this assumption being partially true for highly irradiated planets, if the temperature of the atmosphere at the region where stellar irradiation is absorbed is way lower than the effective temperature of the star, the two radiation fields are mostly decoupled. If isotropic irradiation is assumed, the temperature profile is given by:

$$T^4 = \frac{3T_{\text{int}}^4}{4} \left[ \frac{2}{3} + \tau \right] + \frac{3T_{\text{eq}}^4}{4} f \left[ \frac{2}{3} + \frac{1}{\gamma\sqrt{3}} + \left( \frac{\gamma}{3} - \frac{1}{\gamma\sqrt{3}} \right) e^{-\gamma\tau\sqrt{3}} \right] \quad (7)$$

where  $T_{\text{int}}$  is the planetary internal temperature,  $T_{\text{eq}}$  is the atmosphere equilibrium temperature,  $f$  is a redistribution coefficient which is  $f = 1$  for the substellar point and  $f = 1/4$  for an average over the entire surface,  $\tau$  is the optical depth, and  $\gamma$  is the ratio between visual and infrared mean opacities.

#### 3.3 Madhusudhan & Seager (2009) and simplified Two-layer model

This parametric P-T profile, proposed by [Madhusudhan & Seager \(2009\)](#), assumes that the diffusion approximation still holds in the layers barely above the radiative-convective boundary and that incident stellar radiation is absorbed higher up in the atmosphere, leading to a nearly isothermal temperature structure in the layers immediately above the radiative-convective boundary. Above this isothermal region, the diffusion approximation breaks down as the pressure and optical depth drop significantly, allowing for thermal inversion layers to form in the stratosphere. The atmosphere is divided into three regions, parametrized by the following equations:

$$\begin{aligned} P_0 < P < P_1 : \quad P &= P_0 e^{\alpha_1 (T - T_0)^{\beta_1}} & \text{Layer 1,} \\ P_1 < P < P_3 : \quad P &= P_2 e^{\alpha_2 (T - T_2)^{\beta_2}} & \text{Layer 2,} \\ P > P_3 : \quad T &= T_3 & \text{Layer 3.} \end{aligned} \quad (8)$$

The model has nine free parameters, but  $\beta_1 = \beta_2 = 0.5$  are set empirically, and  $P_0 = 10^{-6}$  bar as optical depths above this pressure typically become so low that the layers of the atmosphere are nearly transparent to incoming and outgoing radiation. Imposing continuity in the layers boundaries, the model can be reduced to six free parameters:  $\alpha_1$ ,  $\alpha_2$ ,  $T_0$ ,  $P_2$ ,  $P_3$  and  $T_3$ . The upper layer corresponds to a "mesosphere" and the middle layer to a "stratosphere" where thermal inversions can be present.

As mentioned by [Madhusudhan & Seager \(2009\)](#), layer 3 is present in the atmosphere of hot Jupiters where the radiative-convective boundaries occur deep in the atmosphere where pressures are higher than 100 bar. However, for cooler planets, the radiative-convective boundary occurs at lower pressures, causing layer 3 to be presumably absent, with layer 2 extending deeper in the atmosphere. Having this in mind, we also considered a simplified version of the parametric P-T profile, consisting of the only two upper layers, corresponding to the mesosphere and the stratosphere. The modified model has only four free parameters:  $\alpha_1$ ,  $\alpha_2$ ,  $T_0$ ,  $P_2$ , and  $T_2$ .

### 4 PARAMETRIC CLOUDS MODELS

Clouds play a critical role in planetary atmospheres. The energy budget of planetary atmospheres is determined by the balance between

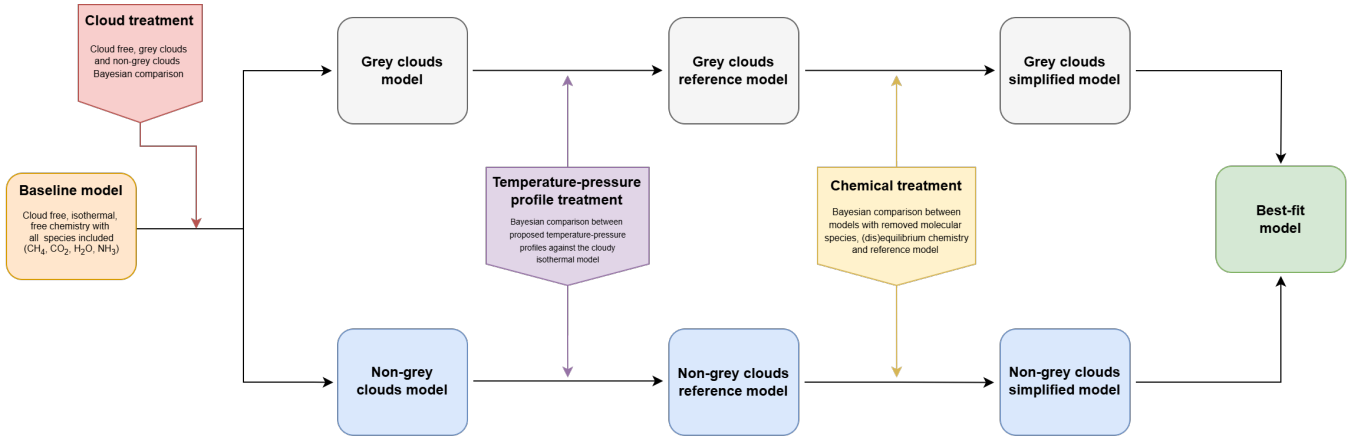


**Figure 2.** Schematic representation of the retrieval workflow used to evaluate different atmospheric models for K2-18b. The process begins with a baseline model, followed by successive treatments for cloud properties, temperature-pressure profiles, and chemistry treatments. Each step refines the model until the best-fit configuration is obtained. Adapted from Figure 2 of [Lueber, Anna et al. \(2024\)](#).

radiative loss of thermal energy from the planetary interior and atmosphere, and the absorbed incident stellar radiation. Clouds are an important source of planetary albedo by reflecting short wave radiation back to space, reducing the available stellar energy for heating the atmosphere. They also play a role in the greenhouse effect by reducing the amount of long wave radiation that escapes from the lower region of the atmosphere, thus increasing the temperature in the deeper regions and attenuating atmospheric cooling. Both effects have a large impact on planetary climate, habitability, and thermal evolution. Clouds also impact the observed spectrum, as cloud particles span a wide range of sizes, causing their absorption and scattering cross sections to exhibit a continuum character and cover a broad spectral range. This results in a partial or complete muting effect on the spectral features, reducing the contrast between the spectral lines and the surrounding continuum, making them weaker and more challenging to detect.

The terms "clouds" and "hazes" are often used interchangeably, but in the context of exoplanet atmospheres, they have different physical processes attributed to their formation. Clouds refer to those condensates that form when the partial vapour pressure of the condensing species exceeds its saturation vapour pressure, generally caused by adiabatic cooling, leading to the nucleation and growth of condensation cloud particles. On the other hand, hazes refer to the condensate species produced via photochemistry in the uppermost regions of the atmosphere, where high-energy radiation ionizes and dissociates simple molecules and can form new condensate molecules.

The overall opacity contribution of these effects on a planetary atmosphere depends on the clouds composition, altitude, vertical and horizontal distribution, particle size distribution, and various micro-physical processes such as nucleation, condensation, and sedimentation. Given the complexity of these processes, simplified models and parametrizations have been developed to account for the impact of clouds in exoplanet atmospheres, where observational data is significantly limited compared to that of Solar System planets.

#### 4.1 Opaque grey cloud deck

In this model, clouds are modelled as a single layer of constant opacity not dependent on wavelength. The cloud deck is assumed to be semi-infinite, meaning that the cloud-bottom pressure extends to the lower boundary of the model domain, effectively blocking any

radiation from reaching or escaping from deeper layers. Since the opacity is wavelength-independent, this model does not account for Mie or Rayleigh scattering effects, making it a useful approximation for high-altitude clouds. The cloud base pressure  $P_{\text{base}}$  is the key free parameter for this model, as it determines the maximum depth at which the atmosphere can be probed.

#### 4.2 Non-grey clouds

In more sophisticated models, clouds are treated as non-grey, meaning their opacities vary with wavelength due to the intrinsic absorption and scattering properties of the cloud particles. Instead of assuming a constant opacity, these models use wavelength-dependent optical properties derived from laboratory measurements and theoretical calculations of candidate condensate species.

The [Ackerman & Marley \(2001\)](#) picture provides a physically motivated framework for describing cloud formation and distribution in exoplanetary atmospheres, balancing condensation, vertical mixing, and sedimentation. As a consequence of vertical mixing, parametrized by the eddy diffusion coefficient  $K_{zz}$ , particles are transported upward into the atmosphere, counteracting gravitational settling, which causes them to fall. A sedimentation efficiency parameter  $f_{\text{sed}}$  is introduced, which quantifies the efficiency of cloud particles settling:

$$-K_{zz} \frac{\partial q_t}{\partial z} - f_{\text{sed}} w^* q_c = 0 \quad (9)$$

where  $K_{zz}$  is the eddy diffusion coefficient,  $q_t$  is the mixing ratio of condensate and vapour,  $q_c$  is the mixing ratio of condensate and  $w^*$  is the mass-weighted sedimentation velocity. Higher values of  $f_{\text{sed}}$  correspond to a more efficient sedimentation, leading to thinner clouds, while lower values correspond to more vertically extended clouds. In this model, cloud formation occurs when the partial vapour pressure of a condensing species equals its saturation vapour pressure, leading to condensate formation and subsequent gravitational settling. As a result of this process, atmospheric layers above the cloud become depleted in the elements that take part in the condensate. The model assumes that cloud particles follow a log-normal size distribution in each layer above the condensation level, and that the mean particle size is controlled by  $K_{zz}$  and  $f_{\text{sed}}$  parameters.



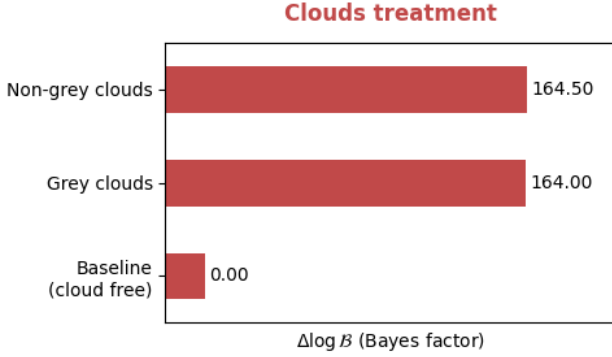


**Figure 3.** Bayes factor comparison of cloud treatments in the atmospheric retrieval of K2-18b. The baseline model consists of a cloud-free atmosphere, while alternative models incorporate grey and non-grey cloud parametrizations.

## 5 CHEMICAL MODELS

One of the main goals of atmospheric characterization is to determine the presence, diversity and abundances of the different chemical species present in the atmosphere. Multiple interactions and mechanisms need to be accounted for to build a model that fully captures all the chemistry structure that shapes the atmosphere spectrum. Photochemistry, vertical and horizontal transport processes, clouds feedback, planetary interior outgassing and thermochemical reactions are just some of the very processes that can affect the detection of chemical species in a planetary atmosphere. A model that accounts for the interplay between these processes is said to be self-consistent. However, given the formidable complexity of the self-consistent models, simplified treatments need to be considered in order to be able to describe the chemical properties encoded in the observed spectrum.

### 5.1 Free chemistry

The simplest model for the chemical structure of an atmosphere. Chemical mass fractions of each species are vertically constant and their value can be arbitrarily defined. Free chemistry serves as a first approximation for chemical modelling, particularly in cases where complex models introduce strong degeneracies or when data quality does not allow for more detailed assumptions.

### 5.2 Equilibrium and disequilibrium chemistry

Assuming that the vertical transport of material can be modelled as a diffusion process parametrized by the eddy diffusion coefficient  $K_{zz}$ , the time it takes for material to be mixed over one scale height of the atmosphere  $H$ , i.e. the dynamical timescale  $t_m$ , is defined as:

$$t_m = \frac{H^2}{K_{zz}} \quad (10)$$

The chemical time scale  $t_c$  of a chemical species quantifies how fast the species reacts or is produced/destroyed in the atmosphere given the local thermodynamic conditions, being generally shorter at higher temperatures and higher pressures (which increases the rate of chemical reactions). The chemical structure of the atmosphere is then controlled at each layer by the relation between these two timescales. If  $t_c$  is much shorter than  $t_m$ , chemical reactions occur faster than vertical mixing processes, allowing the atmosphere to remain in local

thermodynamical equilibrium (LTE). Chemical abundances are then determined by pressure, temperature, and elemental composition of the atmosphere.

On the other hand, if  $t_m$  is shorter than  $t_c$ , chemical species are vertically transported and mixed before reaching equilibrium, shifting away the abundances of the chemical species from their LTE values. This disequilibrium process can lead to a vertical homogenization of the abundances of chemical species above the level where the dynamical mixing timescale dominates over the chemical timescale, which is known as the *quenching* approximation. Vertical mixing processes are not the only source of disequilibrium in the atmosphere. Incident stellar flux of high energy is absorbed in the upper atmosphere and induces the photodissociation of base molecules transported from the deep atmospheric regions, driving the production of radicals that react to form new chemical species. The photochemical timescale  $t_{\text{phot}}$  can dominate over the dynamical and chemical timescales, which can lead to sharp vertical abundance gradients of the photochemical-induced species in the upper regions of the atmosphere.

## 6 RETRIEVALS SETUP

The atmosphere of K2-18b is modelled as a one-dimensional, plane-parallel atmosphere in hydrostatic equilibrium, consisting of 120 layers spanning a range of pressures from 100 bar to 1  $\mu$ bar. Atmospheric retrievals were conducted using the retrieval utility of the *petitRADTRANS* (Mollière et al. 2019) radiative transfer code. We performed the retrievals based on K2-18b's high-resolution transmission spectra reported by Madhusudhan et al. (2023), consisting of the NIRISS SOSS spectrum in the wavelength range of 0.9–2.8  $\mu$ m and the NIRSPEC G395H spectrum in the 2.8–5.2  $\mu$ m range (see Figure 1). Gas, clouds and collision-induced absorption opacities used in the retrievals are provided in the opacity database of *pRT* and consist of the following molecules: CH<sub>4</sub> (Yurchenko, Sergei N. et al. 2017), CO<sub>2</sub> (Yurchenko et al. 2020), H<sub>2</sub>O (Polyansky et al. 2018) and NH<sub>3</sub> (Coles et al. 2019). For the non-grey clouds model, we use clouds of water-vapour liquid condensate from Segelstein (1981). We also consider the H<sub>2</sub>–H<sub>2</sub> (Borysow et al. 2001), and H<sub>2</sub>–He (Borysow et al. 1988), collision-induced absorption opacity contributions.

Since we have to consider multiple thermal profile models, cloud treatments, and molecular species populations in various combinations, we follow a similar workflow as described in Lueber, Anna et al. (2024) for the WASP-39b atmospheric retrieval. Figure 2 illustrates how we conducted our models exploration.

Model comparison is carried out by evaluating the Bayes factor  $\mathcal{B}$ , which is the ratio of the Bayesian evidence between the pair of competing models. In principle, this factor allows us to discern the model that fits the data with the most optimal balance between quality of fit and model complexity. Additionally, we follow the "Bayesian significance" interpretation from Table 2 of Trotta (2008), which provides a comprehensive conversion between frequentist significance levels and Bayes factor values:  $\log \mathcal{B} \sim 1$  corresponds to a "weak at best" detection,  $\log \mathcal{B} \sim 2.5$  to a "moderate at best" detection, and  $\log \mathcal{B} \geq 5$  to a "strong at best" detection. All detections significances have an intrinsic statistical uncertainty of  $\sim 0.1\sigma$  owing to the Bayesian evidence obtained through the nested sampling algorithm (Trotta 2008).

### 6.1 Retrievals workflow

We begin with an isothermal, cloud-free model with vertically uniform chemical abundances, including all four chemical species (CH<sub>4</sub>,

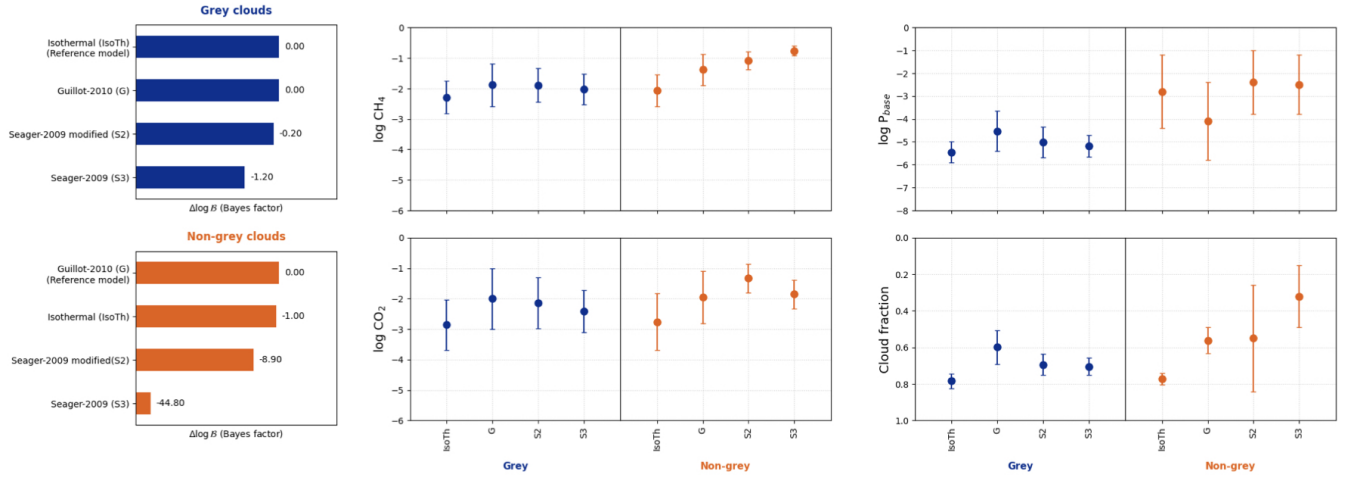


**Figure 4.** Bayesian model comparison for different thermal models with grey (in blue) and non-grey (in orange) cloud treatments. In the left-most panels,  $\log \mathcal{B}$  is compared for each model with respect to the reference for grey and non-grey set of retrievals. On the right panels, values of the  $\text{CH}_4$  and  $\text{CO}_2$  abundances, log pressure of base clouds, and cloud fraction are shown for both clouds parametrizations. In the grey clouds case, isothermal is favoured over the rest of retrievals and therefore is chosen as the reference. For the non-grey models, the Guillot (2010) G model is favoured by the data, and S2 and S3 models from Madhusudhan & Seager (2009) are strongly disfavoured.

$\text{CO}_2$ ,  $\text{H}_2\text{O}$  and  $\text{NH}_3$ ), which we refer to as the baseline model. Then, grey and non-grey cloud treatments with the same thermal and chemical configuration are compared to the cloud-free model, resulting in the cloud-free model being disfavoured via Bayesian model comparison, favouring cloudy models (see Figure 3). For each isothermal cloudy model, we vary the temperature-pressure using the semi-ideal Guillot (2010) profile, as well as the full and simplified profiles from the Madhusudhan & Seager (2009) parametric model, and compare them to the isothermal case. For each set of retrievals (with either grey or non-grey clouds), the model with the highest Bayes factor is selected and designated as the reference model.

Once the temperature-pressure profile has been selected, we assess the chemistry treatment by evaluating six different models. Each one of the four molecular species is individually removed from the reference model, one at a time, to test its impact on the resulting fit. If removing a species increases the Bayesian evidence, it is excluded from the model. Conversely, if removing a species decreases the Bayesian evidence, the species is included in the model only if the logarithm of the Bayes factor exceeds unity. Following this approach, we are able to identify the model with the least number of chemical species necessary to explain the data.

To determine the equilibrium abundances of the retrieved species at each atmospheric pressure layer, volume mixing ratios are interpolated from precomputed chemical abundances tables provided by the *pRT* package. Disequilibrium chemistry is implemented using the quenching approximation, retrieving the quenching pressure above which  $\text{CH}_4$  and  $\text{H}_2\text{O}$  abundances remain vertically constant. For both equilibrium and disequilibrium models, the retrieved parameters are not the individual chemical mixing ratios of each species, but rather the atmospheric metallicity  $\text{Fe}/\text{H}$  and the carbon-to-oxygen ratio  $\text{C}/\text{O}$ , which govern the elemental abundances of the primary carbon and oxygen-bearing molecules of the atmosphere. Considering these chemical models, we identify the model that best fits the data with the fewest free parameters, which we refer to as the simplified model. Finally, we conduct Bayesian model comparison between the simplified models corresponding to the grey and non-grey cloud treatments, determining the best fit to the transmission spectrum of K2-18b.

## 7 RESULTS

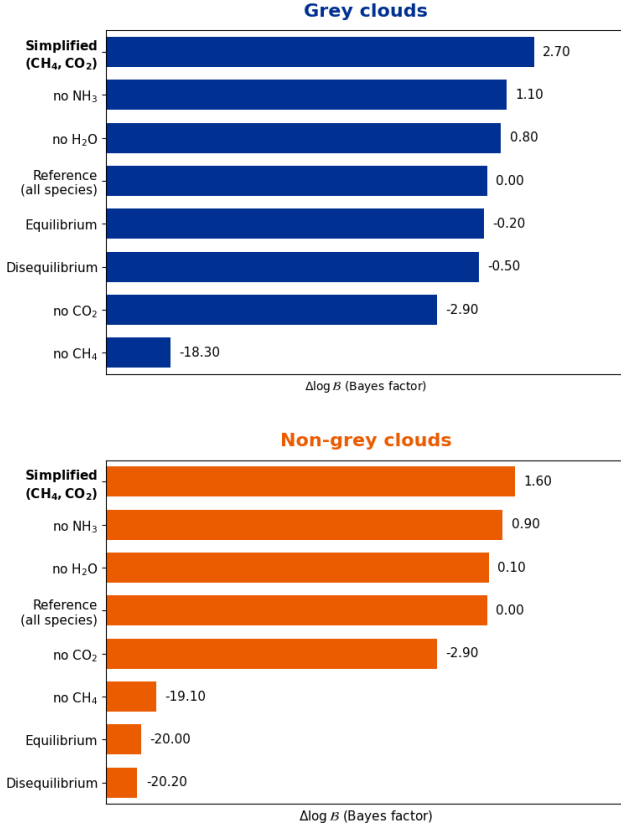
### 7.1 Clouds treatment

Figure 3 shows the Bayesian model comparison between cloud-free and cloudy atmospheres, representing the initial step in the retrieval workflow outlined in Figure 2. The cloud-free model is clearly ruled out by the data in  $\log \mathcal{B} \sim 164$  which corresponds to a significance greater than  $5\sigma$ , indicating that cloudy models are strongly favoured over a clear atmosphere, in agreement with Madhusudhan et al. (2023). For grey and non-grey cloud models, the comparison yields  $\log \mathcal{B} < 1$  indicating that both approaches explain equally well the observed data.

### 7.2 Thermal profiles

Figure 4 shows the results of a set of retrievals exploring how a different choice for the pressure-temperature profile affects the resulting values for the key model parameters, and how those models compare with the corresponding reference model. For both grey and non-grey cloud parametrizations, and considering the full set of chemical species, we evaluated the Guillot (2010) temperature-pressure profile, the Madhusudhan & Seager (2009) three-layer parametric profile, and a modified version of the latter in which the isothermal deepest layer is absent. From now on, we denote these as the G, S3 and S2 models, respectively.

For the grey cloud models, retrieved abundances for  $\text{CH}_4$  and  $\text{CO}_2$  are in the range of  $10^{-2}$  to  $10^{-3}$ , while  $\text{H}_2\text{O}$  and  $\text{NH}_3$  abundances are found between  $10^{-5}$  and  $10^{-7}$ , suggesting a predominance of the former chemical species, which is a priori in agreement with the results of previous studies. The retrieved cloud base pressure  $\log P_{\text{base}}$ , around  $10^{-5}$  for all the grey clouds models, indicates the presence of high-altitude clouds that could partially mute the absorption features of certain chemical species, possibly leading to an underestimation of their retrieved molecular abundances. For instance, in the case of the isothermal profile, the retrieved high cloud coverage fraction of  $\phi = 0.78 \pm 0.04$ , along with the derived cloud base pressure of  $\log P_{\text{base}} = -5.45 \pm 0.45$  bar, could explain the relatively low molecular abundances of  $\text{CH}_4$  and  $\text{CO}_2$  compared to other profiles.



**Figure 5.** Bayesian evidence ( $\log \mathcal{B}$ ) for different chemical scenarios under grey (top) and non-grey (bottom) cloud treatments. The reference model includes all considered chemical species. Removing  $\text{NH}_3$  and  $\text{H}_2\text{O}$  increases Bayesian evidence in both cases, while excluding  $\text{CH}_4$  significantly decreases it, indicating a strong detection. Equilibrium and disequilibrium chemistry models are strongly disfavoured, particularly under non-grey clouds. The simplified model, including only  $\text{CH}_4$  and  $\text{CO}_2$ , provides the highest Bayesian evidence.

The upper-left panel of Figure 4 presents the Bayesian comparison of the four grey clouds models with different thermal profiles. The S3 model is ruled out by the data, with a Bayes factor of  $\log \mathcal{B} = -1.20$  compared to the models with the highest factor. Comparing the S2 and G models to the isothermal model, we find  $\log \mathcal{B} = -0.2$  and  $\log \mathcal{B} = 0$  respectively, indicating that all three models explain the observed spectrum equally well. However, applying the Occam's Razor principle, we choose the isothermal model as the reference for the grey clouds treatment, as it has the fewest free parameters and lowest complexity.

For the set of non-grey clouds retrievals, the isothermal temperature profile yields molecular abundances similar to the grey clouds case, with retrieved abundances of  $\log X_{\text{CH}_4} = -2.07 \pm 0.52$ ,  $\log X_{\text{CO}_2} = -2.76 \pm 0.93$ ,  $\log X_{\text{H}_2\text{O}} = -5.80 \pm 1.50$  and  $\log X_{\text{NH}_3} = -6.40 \pm 1.10$ . The G model yields similar abundances for  $\text{H}_2\text{O}$  and  $\text{NH}_3$ , but with  $\log X_{\text{CH}_4} = -1.38 \pm 0.51$  and  $\log X_{\text{CO}_2} = -1.96 \pm 0.86$ . The S2 and S3 models yield relatively high  $\text{CH}_4$  and  $\text{CO}_2$  abundances, with  $\log X_{\text{CH}_4} = -1.08 \pm 0.29$  and  $\log X_{\text{CO}_2} = -1.33 \pm 0.47$  for S2, and  $\log X_{\text{CH}_4} = -0.76 \pm 0.16$  and  $\log X_{\text{CO}_2} = -1.85 \pm 0.47$  for S3. For  $\text{H}_2\text{O}$  abundance, S2 and S3 models yield similar values for  $\log X_{\text{H}_2\text{O}}$  of  $-5.70 \pm 1.50$  and  $-6.20 \pm 1.30$  respectively, but strongly differ for the  $\text{NH}_3$  abundances, for which S2 yields a value of  $\log X_{\text{NH}_3} = -6.53 \pm 0.91$  while S3 yields  $\log X_{\text{NH}_3} = -0.99 \pm 0.12$ ,

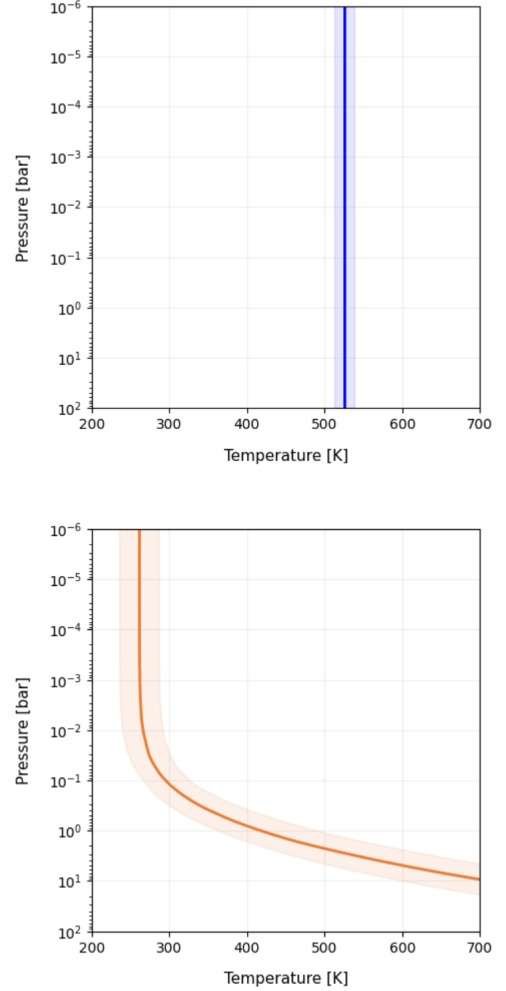


**Figure 6.** Retrieved temperature-pressure profiles of the simplified models. The top panel shows the isothermal temperature profile of the simplified grey clouds model. The bottom panel shows the semi-ideal Guillot temperature-pressure profile of the non-grey clouds simplified model. In both cases, the solid line represents the best-fit profile, while the shaded region denotes the  $1\sigma$  uncertainty range derived from Monte Carlo sampling of parameter bounds.

suggesting a rich  $\text{NH}_3$  atmosphere in agreement with the mini-Neptune scenario for K2-18b, as proposed by Wogan et al. (2024).

The inferred cloud base pressure for the non-grey models suggests the presence of clouds at low altitudes for the isothermal, S2, and S3 models, and in the mid-atmosphere for the G model. This could explain the high uncertainties for this parameter compared to the high-altitude clouds of the grey cloud models, as deeper regions of the atmosphere experience higher opacity, leading to a reduced contribution to the observed spectrum. The low retrieved gas-phase abundance for  $\text{H}_2\text{O}$  is consistent with a water-vapor cloud layer in the deep region of the atmosphere. As  $\text{H}_2\text{O}$  gas-phase molecules are transported upward from the deepest layers, they start to condense at the cloud base level, leading to a progressive depletion of water vapour in the upper atmosphere. For the S2 and S3 models, the retrieved abundances of  $\text{CH}_4$  and  $\text{CO}_2$ , combined with the presence of potentially low-altitude clouds and a low cloud coverage fraction that does not reflect sufficient stellar radiation back into space, suggest a carbon-rich atmosphere with a potentially strong greenhouse effect. This could lead to significant atmospheric warming, potentially

Parameter	Prior Range	Simplified - grey clouds (isoTh)	Simplified non-grey clouds (G)
Temperature (K)	(0, 1000)	524 ± 23	—
$T_{\text{int}}$ (K)	(0, 600)	—	294 ± 54
$T_{\text{eq}}$ (K)	(0, 600)	—	158 ± 94
$\gamma$	(0.01, 10)	—	0.3 ± 1.1
$\log \kappa_{\text{IR}}$ ( $\text{cm}^2 \text{g}^{-1}$ )	(-3, 1)	—	-2.16 ± 0.49
$\log K_{zz}$ ( $\text{cm}^2 \text{s}^{-1}$ )	(4, 12)	—	9.59 ± 0.97
$f_{\text{sed}}$	(0.001, 1)	—	0.028 ± 0.074
$\sigma_{\text{Inorm}}$	(1.05, 3)	—	2.07 ± 0.60
$\log X_{\text{cloud,base}}$	(-6, 0)	—	-1.04 ± 0.40
$\log P_{\text{base}}$ (bar)	(-5, 0)	-5.49 ± 0.47	-4.0 ± 1.7
Cloud coverage $\phi$	(0, 1)	0.78 ± 0.04	0.55 ± 0.07
$\log X_{\text{CH}_4}$	(-8.0, -0.1)	-2.35 ± 0.56	-1.34 ± 0.43
$\log X_{\text{CO}_2}$	(-8.0, -0.1)	-2.83 ± 0.78	-1.71 ± 0.51

**Table 1.** Retrieved parameters for the best-fit simplified models of K2-18b. The table lists the free parameters, their prior ranges, and the retrieved values with uncertainties for both the grey and non-grey clouds simplified models.

shifting the cloud base to higher altitudes where temperatures are low enough for water-vapour condensation.

In the bottom left-most panel of the Figure 4, the four thermal models for the non-grey cloud treatment are evaluated using Bayesian model comparison. The S2 and S3 models are significantly disfavoured, with  $\log \mathcal{B}$  values of -8.90 and -44.80, respectively. The isothermal model is slightly disfavoured compared to G, with a  $\log \mathcal{B} = -1$ . The G model is chosen as the reference model, as it has the highest Bayesian evidence, and when compared with the isothermal profile, the Bayesian evaluation supports the evidence in favour of the G profile. The small  $\log \mathcal{B}$  difference between the G and isothermal models suggests that while G is preferred, the isothermal model still provides a relatively reasonable fit. In contrast, the strong negative  $\log \mathcal{B}$  values for S2 and S3 indicate that these models fail to explain the data as effectively as the G model.

### 7.3 Chemistry treatment

Figure 5 shows the results of the chemistry exploration for both grey and non-grey cloud treatments. For the grey cloud models, removing  $\text{H}_2\text{O}$  from the reference model increased the Bayesian evidence, resulting in  $\log \mathcal{B} = 0.8$  relative to the model with the full set of chemical species. Similarly, removing  $\text{NH}_3$  improves the fit, yielding  $\log \mathcal{B} = 1.1$ . In contrast, when  $\text{CO}_2$  is removed, the Bayesian evidence decreases to  $\log \mathcal{B} = -2.9$ , suggesting a detection significance of about  $3\sigma$  following the [Trotta \(2008\)](#) interpretation. The removal of  $\text{CH}_4$  has a stronger effect, decreasing the Bayesian evidence by  $\log \mathcal{B} = -18.30$ , corresponding to a detection significance greater than  $5\sigma$ . These results align with those from [Madhusudhan et al. \(2023\)](#), which reported detection significances for  $\text{CH}_4$  and  $\text{CO}_2$  of  $5\sigma$  and  $3\sigma$  respectively.

We also explored both equilibrium and disequilibrium chemistry models. Under chemical equilibrium treatment, we retrieved a mildly super-solar metallicity of  $[\text{Fe}/\text{H}] = 0.2$  and a carbon-to-oxygen ratio  $\text{C}/\text{O} = 0.66$ , while for disequilibrium we found a higher metallicity of  $[\text{Fe}/\text{H}] = 0.48$ , an increased  $[\text{C}/\text{O}] = 0.74$ , with a quenching pressure for water and methane of  $\log P_{\text{quench}} = -1.6 \pm 2.6$ . These findings suggest a substantial  $\text{H}_2$ -dominated atmosphere with a moderate enrichment in heavy elements, as retrieved values are intermediate between those of gas giants and ice giants, indicating a composition richer than Jupiter and Saturn but less enriched than Neptune and Uranus. The simplified model, which includes only  $\text{CH}_4$  and  $\text{CO}_2$ , represents the model with the minimal set of chemical species required to explain the data. This model exhibits  $\log \mathcal{B} = 2.70$  com-

pared to the reference model, which includes all four chemical species considered.

In the case of non-grey clouds treatment, both equilibrium and disequilibrium chemistry are strongly disfavoured by the model, leading to a decrease of Bayesian evidence with  $\log \mathcal{B} = -20$  for the equilibrium case and  $\log \mathcal{B} = -20.2$  for the disequilibrium case. The removal of  $\text{NH}_3$  and  $\text{CO}_2$  increases the Bayesian evidence, yielding  $\log \mathcal{B} = 0.9$  and  $\log \mathcal{B} = 0.1$  respectively, following the same trend observed for the grey clouds treatment. Consequently, these species are not included in the simplified model, as they are not necessary to fit the data. Similarly, as in the grey clouds treatment, the Bayes factor for  $\text{CH}_4$  removal is found to be  $\log \mathcal{B} = -18.30$ , implying a detection significance greater than  $5\sigma$ , while the removal of  $\text{CO}_2$  yields a  $\log \mathcal{B} = -2.9$ , corresponding to a detection significance of  $3\sigma$ , consistent with the findings of [Madhusudhan et al. \(2023\)](#).

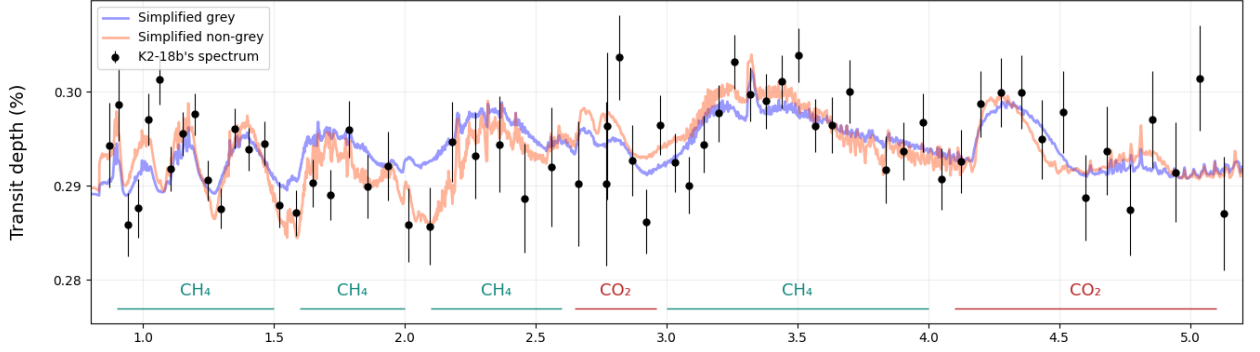
### 7.4 Simplified models

Table 1 summarizes the list of free parameters, prior ranges and best-fit values, of the grey and non-grey simplified models for the atmospheric retrieval of K2-18b. For the grey clouds model, we derive a  $\text{H}_2$ -rich atmosphere with significant abundances of methane  $\log X_{\text{CH}_4} = -2.35 \pm 0.78$  and carbon dioxide  $\log X_{\text{CO}_2} = -2.83 \pm 0.78$ , a retrieved temperature of  $524 \pm 23$  K, and a grey cloud deck at an altitude of  $\sim 10^{-5}$  bar with a cloud coverage factor around 0.78.

The high retrieved temperature could be attributed to several factors. Both  $\text{CH}_4$  and  $\text{CO}_2$  are strong infrared absorbers, significantly influencing the thermal structure by contributing to a moderate greenhouse effect, which increases the retrieved atmospheric temperature. Additionally, the retrieved high-altitude cloud deck at  $\sim 10^{-5}$  bar suggests that deeper atmospheric layers are obscured by optically thick clouds, meaning the retrieval is sensitive only to the upper atmosphere. At these altitudes, physical processes such as photodissociation, photochemical haze formation, and temperature inversions could become dominant, causing the temperature to increase. Top panel of Figure 6 shows the derived temperature-pressure profile of the simplified grey clouds model.

For the non-grey clouds case, we found an internal temperature of  $T_{\text{int}} = 294 \pm 54$  K and an equilibrium temperature of  $T_{\text{eq}} = 158 \pm 94$  K. The retrieved equilibrium temperature is quite low compared to the expected equilibrium temperature for Sub-Neptune exoplanets (which is expected to be between 200 – 300 K ([Benneke et al. 2019](#))), but given the large uncertainty, the retrieved  $T_{\text{eq}}$  could still be consistent with expectations. Retrieved abundances for methane





**Figure 7.** Comparison of simplified atmospheric models for both grey and non-grey clouds treatments. The data in black corresponds to the low-resolution transmission spectrum of K2-18b. The non-grey model (orange) shows stronger absorption features, while the grey model (blue) produces a flatter spectrum. Key spectral features regions of CH<sub>4</sub> and CO<sub>2</sub> are indicated [Madhusudhan et al. \(2023\)](#). The spectral feature around  $\sim 4.2 \mu\text{m}$  makes possible the detection of CO<sub>2</sub>. Both fits report a reasonable fit to the data with a reduced  $\chi^2_{\nu} = 1.08$

$\log X_{\text{CH}_4} = -1.34 \pm 0.43$  correspond to a volume mixing ratio of about  $\sim 1\%$ , and for carbon dioxide  $\log X_{\text{CO}_2} = -1.71 \pm 0.51$  correspond to a mixing ratio of  $\sim 0.1\%$ , which is lower compared to the mixing ratio of  $\sim 1\%$  for CO<sub>2</sub> reported by [Madhusudhan et al. \(2023\)](#). The low retrieved pressure for the cloud base  $\log P_{\text{base}}$  suggests water vapour clouds condensation in the upper-mid region of the atmosphere (in align with [Benneke et al. \(2019\)](#)). The retrieved sedimentation parameter  $f_{\text{sed}}$  and standard deviation of the log-normal particle size distribution  $\sigma_{\text{Inorm}}$  suggest very vertically extended clouds with low mean particle size but with a broad distribution of sizes. Inferred value for the eddy diffusion coefficient  $\log K_{zz}$  indicates strong vertical mixing, potentially leading to disequilibrium chemistry and to the upward transport of CH<sub>4</sub> and CO<sub>2</sub> molecules to higher regions of the atmosphere sensible to observations.

Retrieved values for  $\gamma$  and  $\log \kappa_{\text{IR}}$  suggest relatively weak infrared absorption in the atmospheric regions probed by the retrieval. This could be caused by high altitude and optically thick clouds efficiently scattering and reflecting incoming radiation in the visible and infrared, reducing the effectiveness of molecular absorption features in the retrieval. Bottom panel of Figure 6 shows the derived temperature-pressure profile from the retrieved parameters using the semi-ideal parametrization ([Guillot 2010](#)). A Monte-Carlo sampling of the retrieved parameters bounds was conducted to obtain a  $1\sigma$  uncertainty region.

The upper part of the atmosphere, from  $\sim 10^{-2}$  to  $10^{-6}$  bar, is nearly isothermal, suggesting that the atmosphere at these altitudes is in radiative equilibrium. This behavior can be attributed to the presence of high-altitude aerosols or photochemical hazes, which could contribute to absorption and scattering, balancing the radiative cooling and maintaining a nearly constant temperature. At altitudes below  $10^{-2}$  bar, the atmosphere transitions into a steeper temperature gradient, with temperature increasing toward the interior region of the atmosphere, possibly caused by convective processes becoming dominant over inefficient radiative cooling, leading to a steeper temperature gradient. CH<sub>4</sub> and CO<sub>2</sub> molecules could contribute to strong infrared absorption, effectively trapping heat and resulting in an enhanced thermal gradient. Additionally, the high abundance retrieved for the cloud base  $\log X_{\text{cloud,base}}$  could alter the underneath temperature structure by preventing deeper layers of the atmosphere from efficiently cooling by radiative processes. The derived profile

suggests an atmosphere where radiative processes dominate in the upper layers, while convective and infrared absorption effects govern the deeper atmosphere, as is expected for temperate planets. Figure 7 shows the retrieved best fit to K2-18b's spectrum for both grey and non-grey simplified models. The low-resolution spectrum, shown as black data points with error bars, reveals distinct spectral features. The labels at the bottom indicate the contributions of CH<sub>4</sub> and CO<sub>2</sub> spectral features to the overall spectrum (from Figure 3 of [Madhusudhan et al. \(2023\)](#)). Despite both models capturing the overall shape of the transmission spectrum, they predict different transit depths for key spectral features. The non-grey model (orange) generally exhibits stronger variations in transit depth, particularly at wavelengths corresponding to absorption features, whereas the grey model (blue) produces a flatter spectrum, indicative of weaker absorption features. These differences demonstrate the impact of cloud treatment on the inferred fit of the spectrum and on the overall characterization of the atmosphere.

### 7.5 Best-fit model

Conducting Bayesian model comparison between simplified grey and non-grey cloud models, we find that  $\log \mathcal{B} = 0.8$  in favour of the non-grey model, indicating a slight preference for this model as the best fit to the K2-18b data. However, since this difference is not substantial and since the grey cloud model has fewer parameters—leading to lower complexity—it remains a viable model. Additionally, the small Bayes factor suggests that the data do not strongly favour one model over the other, implying that both models provide a reasonable explanation for the observed transmission spectrum within the current uncertainties.

## 8 SUMMARY AND CONCLUSIONS

In this study, we performed a Bayesian retrieval analysis to investigate the atmospheric properties of the sub-Neptune exoplanet K2-18b, focusing on the role of clouds, the thermal structure, and the chemical composition. Our findings highlight several important features concerning the impact of grey and non-grey cloud treatment on the derived atmospheric structure and its properties.

Our Bayesian analysis finds that a cloud-free atmosphere for K2-18b is strongly disfavoured, as it fails to reproduce the observed spectrum. Cloudy models significantly improve the resulting fit, indicating that cloud opacity plays a crucial role in shaping the atmospheric spectrum. The comparison between grey and non-grey models reveals that non-grey clouds provide a slightly better representation of the spectrum by allowing for wavelength-dependent scattering effects that impact the transit depth variations due to characteristic spectral features.

The derived temperature-pressure profile for each cloud treatment suggests different atmospheric properties. The grey clouds model shows evidence in favour of a thermal structure with constant temperature along the vertical direction, suggesting the absence of significant temperature gradients in the atmosphere or the existence of processes that compensate for the atmospheric radiative cooling. Conversely, the non-grey model is consistent with a nearly isothermal behavior in the upper atmosphere and a temperature gradient in the lower layers, which aligns more closely with the expected real structure of an atmosphere. This finding highlights the necessity of a wavelength-dependent parametrization for the clouds to accurately constrain the thermal structure of K2-18b.

Our evaluation of chemistry treatments resulted in the detection of methane (CH<sub>4</sub>) and carbon dioxide (CO<sub>2</sub>) with detection significances of  $5\sigma$  and  $3\sigma$ , respectively. These findings are in alignment with the results reported by Madhusudhan et al. (2023) for the same molecules. No significant evidence was found for water (H<sub>2</sub>O) and ammonia (NH<sub>3</sub>), in agreement with previous studies. Retrieved abundances for CH<sub>4</sub> and CO<sub>2</sub> vary depending on the assumed cloud treatment, suggesting an important relation between cloud properties and molecular absorption features.

The conducted Bayesian model comparison workflow resulted in one best-fit atmospheric model for each cloud treatment. The grey clouds model serves as a basic approximation that possibly underestimates the molecular abundances of detected molecules due to the inferred high-altitude clouds and its uniform treatment of cloud opacity. On the other hand, the non-grey model better reproduces the observed spectrum by including a more consistent representation of cloud scattering and absorption.

Finally, our analysis demonstrates the critical role of cloud modelling, thermal structure assumptions, and chemistry treatment in retrieving the atmospheric properties of K2-18b. Our findings align with previous studies regarding the detection of carbon-bearing molecules in the planet's atmosphere, confirming the presence of methane CH<sub>4</sub> and carbon dioxide CO<sub>2</sub>. However, the question of whether K2-18b's spectrum is best explained by a Hycean world scenario, a mini-Neptune, a rocky planet, or even a lava world remains unresolved. Current observations are not yet definitive due to significant uncertainties and the lack of spectral data in relevant wavelength ranges, such as the infrared and ultraviolet, which are crucial for constraining atmospheric composition and thermal properties. Future observations with a broader wavelength coverage and improved sensitivity will be essential for refining atmospheric models, constraining its chemical and physical properties, and ultimately determining the true nature of K2-18b.

## REFERENCES

- Ackerman A. S., Marley M. S., 2001, *The Astrophysical Journal*, 556, 872–884
- Batalha N. M., 2014, *Proceedings of the National Academy of Sciences*, 111, 12647
- Benneke B., et al., 2019, *The Astrophysical Journal Letters*, 887, L14
- Borysow J., Frommhold L., Birnbaum G., 1988, *Astrophys. J.; (United States)*, 326
- Borysow A., Jørgensen U. G., Fu Y., 2001, *Journal of Quantitative Spectroscopy and Radiative Transfer*, 68, 235
- Coles P. A., Yurchenko S. N., Tennyson J., 2019, *Monthly Notices of the Royal Astronomical Society*, 490, 4638
- Feroz F., Hobson M. P., Bridges M., 2009, *Monthly Notices of the Royal Astronomical Society*, 398, 1601–1614
- Guillot T., 2010, arXiv: Earth and Planetary Astrophysics
- Lueber, Anna Novais, Aline Fisher, Chloe Heng, Kevin 2024, *A&A*, 687, A110
- Madhusudhan N., Seager S., 2009, *The Astrophysical Journal*, 707, 24–39
- Madhusudhan N., Piette A., Constantinou S., 2021, *The Astrophysical Journal*, 918, 1
- Madhusudhan N., Sarkar S., Constantinou S., Holmberg M., Piette A., Moses J., 2023, *The Astrophysical Journal Letters*, 956, L13
- Mollière P., Wardenier J. P., van Boekel R., Henning T., Molaverdikhani K., Snellen I. A. G., 2019, *Astronomy & Astrophysics*, 627, A67
- Polyansky O. L., Kyuberis A. A., Zobov N. F., Tennyson J., Yurchenko S. N., Lodi L., 2018, *Monthly Notices of the Royal Astronomical Society*, 480, 2597
- Rogers L., 2014, *The Astrophysical Journal*, 801
- Segelstein D., 1981, The Complex Refractive Index of Water. Department of Physics. University of Missouri-Kansas City, <https://books.google.com.co/books?id=S1q0NwAACAAJ>
- Trotta R., 2008, *Contemporary Physics*, 49
- Wogan N., Batalha N., Zahnle K., Krissansen-Totton J., Tsai S.-M., 2024, in AAS/Division for Extreme Solar Systems Abstracts. p. 625.15
- Yurchenko, Sergei N. Amundsen, David S. Tennyson, Jonathan Waldmann, Ingo P. 2017, *A&A*, 605, A95
- Yurchenko S. N., Mellor T. M., Freedman R. S., Tennyson J., 2020, *Monthly Notices of the Royal Astronomical Society*, 496, 5282

This paper has been typeset from a  $\text{\LaTeX}$  file prepared by the author.